applied sciences

MDPI

Article

Synthesis and Characterization of Cerium Oxide Nanoparticles: Effect of Cerium Precursor to Gelatin Ratio

Maria Eleni Ioannou [1], Georgia K. Pouroutzidou [1,2], Iason Chatzimentor [1], Ioannis Tsamesidis [1], Nikoletta Florini [2], Ioannis Tsiaoussis [2], Evgenia Lymperaki [3], Philomela Komninou [2] and Eleana Kontonasaki [1,*]

[1] Department of Prosthodontics, School of Dentistry, Faculty of Health Sciences, Aristotle University of Thessaloniki, 54124 Thessaloniki, Greece
[2] School of Physics, Faculty of Sciences, Aristotle University of Thessaloniki, 54124 Thessaloniki, Greece
[3] Department of Biomedical Sciences, International Hellenic University, 57400 Thessaloniki, Greece
* Correspondence: kont@dent.auth.gr

Abstract: Hemocompatible nanoparticles with reactive oxygen species (ROS) scavenging properties for titanium implant surface coatings may eliminate implant failure related to inflammation and bacterial invasion. Cerium (Ce) is a rare earth element, that belongs to the lanthanide group. It exists in two oxidation states, Ce^{+3} and Ce^{+4}, which contribute to antioxidant, catalytic, antibacterial, and ROS-scavenging properties. The purpose of the present study was to synthesize ceria nanoparticles and to evaluate their hemocompatibility and ROS scavenging properties. The synthesis of Ce-NPs was performed via the sol-gel method, and five different ratios of cerium precursors to gelatin were evaluated. Their characterization was achieved through FTIR, XRD, SEM, and TEM. Hemocompatibility and ROS analysis were evaluated at different concentrations with human erythrocytes. The morphology and size distribution were certified by TEM and the cubic CeO_2 fluorite structure was identified by selected area electron diffraction and high-resolution TEM. The particle size of the lowest Ce concentration presented a mean diameter of 10 nm. At concentrations of <500 μg/mL, no hemolytic effect was observed. At the highest concentrations, no hemolytic behavior was recorded for samples with the highest Ce precursor, which also presented ROS scavenging properties (10–50% reduction in ROS). These properties make those CeO_2 NPs unique candidates as nanofillers or nanocoatings with antibacterial properties.

Keywords: cerium oxide nanoparticles; sol-gel method; spectroscopy; microscopy; hemocompatibility; reactive oxygen species

check for updates

Citation: Ioannou, M.E.; Pouroutzidou, G.K.; Chatzimentor, I.; Tsamesidis, I.; Florini, N.; Tsiaoussis, I.; Lymperaki, E.; Komninou, P.; Kontonasaki, E. Synthesis and Characterization of Cerium Oxide Nanoparticles: Effect of Cerium Precursor to Gelatin Ratio. *Appl. Sci.* **2023**, *13*, 2676. https://doi.org/10.3390/app13042676

Academic Editor: Marilena Carbone

Received: 29 December 2022
Revised: 13 February 2023
Accepted: 16 February 2023
Published: 19 February 2023

Copyright: © 2023 by the authors. Licensee MDPI, Basel, Switzerland. This article is an open access article distributed under the terms and conditions of the Creative Commons Attribution (CC BY) license (https://creativecommons.org/licenses/by/4.0/).

1. Introduction

Nanoscience and nanotechnology are two scientific fields closely connected to each other. According to the National Nanotechnology Initiative (NNI): "Nanotechnology is the understanding and control of matter at dimensions between approximately 1 and 100 nanometers, where unique phenomena enable novel applications" [1]. These phenomena, being attributed to the tiny size, lead to a high surface area to volume ratio and different particle shapes, as well as unique physical, chemical, electronic, mechanical, optical, and biological properties which differ from the properties of their bulk counterparts [2]. The prefix 'nano' is derived from a Greek prefix called 'νάνο' which means dwarf or something that has a tiny size on the order of a nanometer (10^{-9} m) [3].

Numerous methods can be employed for the synthesis of NPs which determine their physicochemical properties involving sol-gel, hydrothermal, precipitation, green synthesis, sonochemical, oxidation polymeric precursor, etc. All of the above are included in two broad categories, top-down and bottom-up methods [4]. In general, bottom up refers to the nanoparticles' synthesis by chemical processes between the atoms, ions, and molecules. It is a method well known as the building-up approach while the final sample is prepared

from the atomic scale. Top-down processes use mechanical means to break down or crush bulk material into smaller pieces to create nanoparticles [5]. The sol-gel technique is the most widely preferred of the rest of the bottom-up synthesis methods due to its simplicity as well as it is a cost-effective and low-temperature synthesis technique friendly to the environment [6,7].

Cerium (Ce) is the most prevalent among rare earth elements. It is the most active member of the lanthanide series with an electronic configuration $[Xe]4f^1 5d^1 6s^2$ [8]. Cerium is a block F, group 3, period 6 element with the atomic number 58 [9]. Cerium has two typical oxidation states, Ce (III) and Ce (IV), although most rare earths exist in trivalent. This facilitates the formation of CeO_2 and Ce_2O_3 and thus it possesses antioxidant and catalytic properties due to its redox behavior [5]. Due to the electrical arrangement of Ce^{3+}–$[Xe]4f^1$ being less resilient than Ce^{4+}–$[Xe]4f^0$, the oxidation state of Ce^{3+} is thought to be unstable in relation to Ce^{4+} [10].

Ceria is a whitish and crystalline substance that turns yellowish when it is impure. Cerium is found in the core of a tetrahedron, with oxygen atoms occupying the four corners. A face-centered cubic (f.c.c.) unit cell with the space group Fm3m and a lattice constant of 0.541134 nm is how it is characterized [10]. The ceria structure is known to create distinct, oxygen-deficient, nonstoichiometric $CeO_{(2-x)}$ oxide structures (with $0 \leq x \leq 0.5$) under reducing circumstances and at high temperatures. Ceria does, however, have the propensity to form distinct compositions at lower temperatures. Ceria's capacity to deliver oxygen and thus create a significant number of vacancies, which accounts for its reductive qualities, which make it easy to construct oxygen-deficient nonstoichiometric phases. The "reduced" structures may easily be changed back to CeO_2 by being exposed to an oxidizing atmosphere while still maintaining their fluorite structure [8,11].

The idea of oxygen vacancy in the lattice structure is the lack of single or numerous oxygen atoms in the unit cell of ceria [12]. The enhanced surface activity is related to cerium's oxygen storage capacity (OSC), which is directly connected to how quickly cerium can alter its oxidation state. Cerium oxide has a dynamic valence and defect structure that may vary suddenly or in reaction to environmental factors including temperature, the existence of other ions, and the partial pressure of oxygen [13]. The ratio of Ce^{3+}/Ce^{4+} and the amount of oxygen vacancies have significant impacts on the nanoceria's capacity to switch between different oxidation states. According to studies, the number of oxygen vacancies increases as cerium oxide nanoparticles decrease in size [14]. Many studies have revealed that cerium oxide nanoparticles, which have a distinctive electron structure, may function as biological antioxidants. It has been suggested that oxygen vacancies at the surface mediate this antioxidant action. Additionally, the ceria nanoparticles' electron defects might not be eliminated following their initial interaction with reactive oxygen species, making them potentially powerful catalysts in a live cell [15]. More oxygen vacancies ensure that oxygen atoms may move around inside the crystal more easily, which encourages redox reactions on the surface and results in great catalytic activity [10].

Due to the ability of nanoceria to interchange between two oxidation states Ce^{3+} and $Ce^{4+,}$ it appears to have a strong antioxidant activity by scavenging ROS. Nanoceria's unique redox characteristic may shield different tissues and organs from biological harm generated by various free radicals or reactive oxygen species (ROS) [5]. Superoxide radicals are common in mammalian cells, however, if their quantity rises, it can further cause several illnesses. Superoxide radical production is typically regulated by the SOD (superoxide dismutase), which finally eliminates the plethora of radicals. Ceria nanoparticles have the ability to mimic the regulation mechanism of SOD, switching between the two oxidation states of +3 and +4 and specifically when the +3/+4 ratio is high [16]. In terms of radical scavenging, the reaction between nanoceria and H_2O_2 can have significant ramifications. This process comprises a catalase-like reaction between H_2O_2 and Ce^{4+}, which reduces Ce^{4+} to Ce^{3+} while simultaneously oxidizing H_2O_2 to molecular O_2, showing the catalase-mimetic activity of ceria. A low Ce^{3+}/Ce^{4+} ratio consequently favors this process [17]. Nanoceria may have an additional, fundamental antioxidant effect as a result of the interac-

tions with superoxide and hydrogen peroxide, which might make it extremely desirable as a biological ROS scavenger. Combining the catalase- and SOD-mimetic activity of nanoceria may result in the display of a biorelated process for nanoceria regeneration [17].

Dental primers/adhesives, resin composite restorative materials, enamel-dentin adhesives, and other compounds with similar chemical compositions make up clinical restorative polymers [18]. Many studies have demonstrated that resin-based restorative materials encourage the development of cariogenic biofilms. Products of dental monomers' decomposition, such as bisphenol A-glycidyl dimethacrylate (BisGMA) and triethylene glycol dimethacrylate (TEGMA), which may alter the metabolic activity of caries-correlated bacteria like *Streptococcus mutans* and increase their multiplication, are responsible for the formation of cariogenic biofilm [19]. Any tooth surface which is frequently exposed to sugar is destroyed by the succeeding cariogenic biofilm [20]. As a result, it affects the development of caries and causes caries around restorations (CARS) at the junction of the restoration and the prepared cavity. CARS is one major factor contributing to the failure of resin composite restorations. Thus, it is imperative to effectively manage the development of CARS in order to increase the success rate of composite resins [21,22]. In a recent study, Varghese et al. reported that incorporating 3 wt.% of CeO_2 NPs into dental composite resulted in >99% potency against *Streptococcus mutans, Streptococcus mitis*, *Streptococcus aureus*, and *Lactobacillus* spp. [20]

In another area of the dental field, infection and inflammation, which suppress healing and soft tissue integration, are often linked to dental implant therapy failures [23]. After being surgically placed into the jawbone, dental implants undergo a process known as osseointegration that causes them to become biologically unified [24]. Preventing implant failures is one of the primary goals of surface modification for Ti-based implants [25]. Synthesizing a biocompatible material that has antibacterial properties increases the ratio of implant success [26]. New biomaterials for biomedical applications (dental implants) should satisfy ISO-10993 requirements to ensure that they are safe and hemocompatible (ASTM-F756). The optimum innovative dental implant materials should have a variety of biological potentials under stress, including anti-inflammatory, antioxidative, angiogenic, and osteogenic properties [26–28]. In fact, it has been shown that cerium oxide nanoparticles behave favorably when they are in contact with erythrocytes. They work as potent antioxidants that dramatically improve damaged red blood cells caused by in vitro hyperthermia (anemia model) by reducing ROS production [29]. Thus, cerium oxide NPs are promising nanoparticles to interact with red blood cells in inflammatory situations where high ROS levels are present. In the study of Li et al., [27] CeO_2 NPs with different nanostructures (nanocube, nanorod, and nano-octahedra) were synthesized through hydrothermal methods, spin-coated on titanium grade IV disks, and evaluated for their hemolytic, anti-inflammatory, and antibacterial properties. Despite differences in their behavior, all NPs presented outstanding antimicrobial potential towards common peri-implantitis pathogens, such as *Porphyromonas gingivalis* and *Fusobacterium nucleatum*. As the different physicochemical properties and degree of crystallinity might affect the antimicrobial, antioxidant, and hemolytic properties of CeO_2 NPs, [30] further research is needed to unravel the optimum materials for all biomedical applications where infection control is critical.

The foremost prevalent bacteria that may create considerable amounts of lactic acid and demineralize teeth are *Streptococcus mutants* and *Lactobacilli* [31]. Patients are more likely to develop caries after placement of fixed orthodontic appliances, due to the enhanced plaque and bacteria accumulation around brackets and bands [32]. This equipment makes it challenging for patients to maintain good oral hygiene, which raises the risk of caries. White spot lesions are caused by demineralization of the enamel (WSL) [33]. Within a month of bonding, WSL can be seen around the brackets, and by the time orthodontic treatment is complete, WSL prevalence has been estimated to reach 50% [34]. A literature investigation on CeO_2 nanoparticles reveals a positive effect against oral microbiota [20].

The antibacterial effectiveness of CeO_2 NPs depends on how well they interact with bacteria through electrostatic attraction to produce ROS, which causes bacterial cell death. These nanoparticles disrupt intracellular processes (DNA replication, mitosis, and cellular respiration) in bacterial cells, which results in the production of ROS and the elimination of both Gram-positive and Gram-negative bacteria [4]. On the other hand, according to Zholobak et al., CeO_2 kills bacteria by a direct or an indirect contact mechanism. Thanks to the electrostatic contact, the positively charged CeO_2 is efficiently adhered onto the bacterial cell. In a direct mechanism, CeO_2 is directly deposited on the bacterial cell, causing damage to the outer cell wall and the formation of intracellular ROS. This contact renders the cellular proteins inert, allowing CeO_2 to enter the bacterial cell and inactivate the enzymes that cause the production of hydrogen peroxide. The resulting intracellular ROS damage to DNA, RNA, and protein eventually led to bacterial cell death [35]. Additionally, the reduction of CeO_2 from Ce^{4+} to Ce^{3+} on the cell surface following oxidation and adsorption of the bacterial wall induces oxidative stress [36]. In indirect contact, CeO_2 interacts most of the time with polysaccharide encapsulated bacteria whereas nanoparticles do not directly contact the cell wall. They react with the space around the bacteria and the resulting products cause more bacterial cell damage. Thus, in this contact, ROS are produced extracellularly and enter through the membrane to harm the bacterial cells by destroying nucleic acids and protein, eventually resulting in cell death [37]. The effectiveness of an antibacterial agent also depends on the CeO_2 nanoparticle concentration. Additionally, when CeO_2 nanoparticles are introduced to *E. coli* bacterial cells, they are immediately taken up by the bacteria, resulting in oxidative stress and bacterial cell death [38]. Although, in general, ROS generation has been correlated with antibacterial properties [39], in some pathogens, ROS can exert opposite results by contributing to increased pathogen burden [40].

An important factor in NPs synthesis is the stabilization of the developed NPs in order to prevent aggregation, which can result in the loss of their nanoscale characteristics and related physicochemical properties [41,42]. Different stabilizers such as carboxymethyl cellulose [43], CTAB, polyethylene glycol [44], polyvinyl alcohol (PVA), polyacrylic acid (PAA) [45], citric acid [46], gelatin [47], etc. have been used for the synthesis of metallic NPs namely CuO, CeO_2, and ZnO. Gelatin is a three-chain helical protein derived from collagen [48]. Gelatin contains positively charged amino groups and negatively charged carboxyl and hydroxyl groups that could provide bonding and stabilization [49,50].

The principal aim of this work was to evaluate the role of the Ce precursor to gelatin ratio on the morphological, crystallographic, and biological properties of CeO_2 NPs that could be applied for surface coating of titanium implants or as fillers in dental composites.

2. Materials and Methods

2.1. Materials

The reactants were $Ce(NO_3)_3 \cdot 6H_2O$ (99.999% trace metals basis), gelatin from porcine skin, and ammonia solution 25% ($\geq$99.99% trace metals basis) from Sigma–Aldrich (St. Louis, MO, USA, now Merck KGaA, Darmstadt, Germany).

2.2. Synthesis of Ceria Nanoparticles

For the synthesis of CeO_2 NPs 0.2 g of gelatin was dissolved in 20 mL double distilled water at 40 °C and stirred for approximately 10 min under magnetic stirring, until the solution became clear. After dissolution of gelatin, different amounts of Cerium Nitrate Hexahydrate ($Ce(NO_3)_3 \bullet 6H_2O$) were added slowly in each synthesis, to get different Ce precursor to gelatin ratios. The amount of cerium precursor, gelatin, water, and the ratio of cerium/gelatin are presented in detail in Table 1. After the addition of the cerium precursor, the solution was stirred vigorously for another 30 min. Following this, ammonia solution was added dropwise until the pH reached 10. After completion of the ammonia addition, the materials were kept under mechanical agitation for 1 h. The prepared solutions were centrifuged for 3 min at 5000 rpm and washed several times with acetone and water. Following this, the sample was heated at 80 °C for 12 h to complete the drying of the

materials. Synthesized materials were ground in a mortar to receive materials in powder form. Finally, the obtained samples were placed in platinum capsules in a high-temperature furnace. The obtained samples (CeO1g, CeO2g, CeO3g, CeO4g, and CeO5g) were heated at 550 °C for 1 h with a heating rate of 1 °C/min [51].

Table 1. Amounts of gelatin, Ce precursor, and solvent along with ratios of Gelatin and Ce precursor.

Samples	Gelatin (g)	Ce Precursor (g)	H_2O (mL)	Gelatin/Ce Precursor	Ce Precursor/Gelatin
CeO1g	0.2	1	20	0.20	5.00
CeO2g	0.2	2	20	0.10	10.00
CeO3g	0.2	3	20	0.07	15.00
CeO4g	0.2	4	20	0.05	20.00
CeO5g	0.2	5	20	0.04	25.00

2.3. Characterization of Ceria Nanoparticles

The presence of functional groups was assessed using Fourier transform infrared spectrometer (FTIR). The crystal structure of CeO_2 nanoparticles was determined by powder X-ray diffraction. The morphology of CeO_2 nanoparticles was studied using a scanning electron microscope (SEM). Shape and size distribution was determined by transmission electron microscopy (TEM) and the particles' diameters were certified by Image J [52]. Over 100 NPs were measured, and the particles' diameter distribution was recorded. Hemolytic activity and ROS scavenging capacity of human red blood cells were also assessed.

All FTIR measurements were performed in the transmittance mode with a Perkin Elmer Spectrum 1000 FTIR spectroscope in the midinfrared region, MIR (4000–400 cm^{-1}) with a resolution of 4 cm^{-1} and 32 scans.

XRD measurements of the samples were carried out with the use of a Rigaku Ultima (Tokyo, Japan) diffractometer with Ni-filtered CuKa radiation (λ = 0.1542 Å) wave radiation. The 2θ angle scan range was 5–75°, the pitch was 0.05°, and the scan speed was 0.05°2θ/s.

Morphological assessment and stoichiometric composition of the samples was carried out with JEOL JSM-7610F Plus, supported by an Oxford AZTEC ENERGY ADVANCED X-act energy dispersive X-ray spectroscopy (EDS) system (JEOL Ltd., Tokyo, Japan). To increase the conductivity of the material and perform microanalysis, NPs were coated with carbon with a thickness of 200 Å.

The microstructure of the CeO1g and CeO5gNPs were investigated up to the atomic scale, by combining TEM imaging, selected area electron diffraction (SAED), and high-resolution TEM (HRTEM). TEM specimens were prepared by the dispersion of a small powder quantity in ethanol followed by ultrasonication for 20 min. Two drops of each solution were dropped onto a carbon-coated Cu grid and left to dry at room temperature. The JEOL JEM Cold Filed Emission Gun (CFEG) TEM/STEM F200 microscope was used and operated at 200 kV, with 0.19 nm point-to-point resolution, equipped with a bottom mounted 9 Mpixel RIO GATAN CMOS camera to acquire the images.

2.4. Hemocompatibility Assay

Red blood cells' (RBCs) hemolytic activity was evaluated after incubation with CeO_2 NPs suspension (stock = 5 mg/mL) prepared with sterile isotonic phosphate buffer saline. CeO_2 NPs were incubated at different concentrations (125, 250, 500, and 1000 μg/mL) for 24 h at 37 °C with a hematocrit of 5%. Erythrocytes without CeO_2 were used as a negative control (Ctrl−) and hemolysis of erythrocytes [as positive control (Ctrl+)] was mechanically induced with distilled water. Then, the supernatant of the samples was obtained after centrifugation previously performed for the same studies [47]. The absorbance value of

haemoglobin at 541 nm was measured with the reference wavelength of 700 nm. The percent of hemolysis was calculated as follows:

$$\text{Hemolysis } \% = \frac{[(sample\ absorbance - negative\ control)}{(positive\ control - negative\ control)]} \times 100\% \quad (1)$$

The results presented were received from six independent experiments performed in triplicate.

2.5. Blood Sample Collection

Fresh human whole blood was collected from healthy volunteer blood donors from the blood donation station of the General Hospital of Naousa (59200, Naousa, Greece). The confidentiality of donors was wholly preserved. Informed consent was obtained from all subjects involved in the study. Good clinical practice guidelines and the Declaration of Helsinki were followed according to the Ethical Committee for the hospital's approval of the study (ID_233205920). Technically, RBCs were separated from plasma as previously described [53].

2.6. Reactive Oxygen Species Levels (ROS) in Erythrocytes

Erythrocyte lysates from the different tested conditions from the hemocompatibility assay were stored and used for the analysis of intracellular reactive oxygen species (ROS) levels. CM-H2DCFDA probe, was used to detect the ROS amounts in erythrocytes as previously described [54]. RBCs treated with various concentrations of CeO_2 NPs were evaluated by measuring the fluorescence of the RBC suspensions. The relative fluorescence was measured with a Tecan fluorometer, where maximal emission was expressed using 3 mM of H_2O_2.

3. Results

3.1. Fourier Transform Infrared Spectroscopy

FTIR spectra of CeO_2 nanoparticles are shown in Figure 1. In the functional group region, there is a broad peak around 3450–3250 cm^{-1} which corresponds to the stretching vibration of the -OH group of water molecules, and a band at 1556 cm^{-1}, which is associated with C-H stretching [55,56]. In the fingerprint region, the peak at 1298 cm^{-1} is characteristic of carbonates species vibration [57], while peaks around 1054 cm^{-1} [58], 680 cm^{-1} [59], and 490 cm^{-1} [60] prove the formation of CeO_2 bands. Ce-O stretching vibrations are shown at the 952 cm^{-1} [61], 844 cm^{-1} [62], 730 cm^{-1} [56], and 424 cm^{-1} [63] regions, respectively.

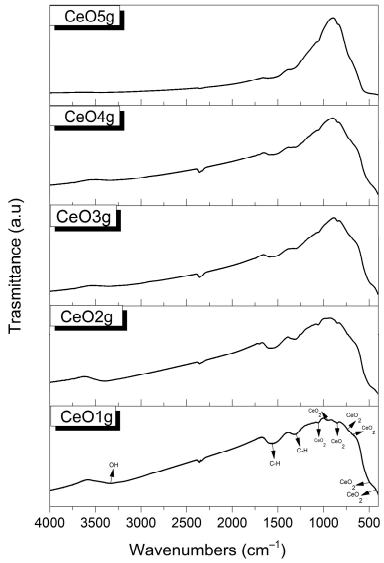


Figure 1. FTIR spectra of CeO_2 nanoparticles.

3.2. X-ray Diffraction Spectroscopy

The XRD patterns of CeO_2 are presented in Figure 2. The peaks are identified using the PDF card #65-5923. Nanoparticle samples have a face center cubic (FCC) structure with lattice parameters a = b = c = 5.404 Å, and $\alpha = \beta = \gamma = 90^\circ$. The diffraction peaks found at 28.6°, 33.1°, 47.5°, 56.4°, 59.1°, and 69.5° correspond to the formation of nano CeO_2 and are associated with hkl (111), (200), (220), (311), (222), and (400) respectively. The absence of impurities implies that pure CeO_2 was produced using the applied sol-gel method.

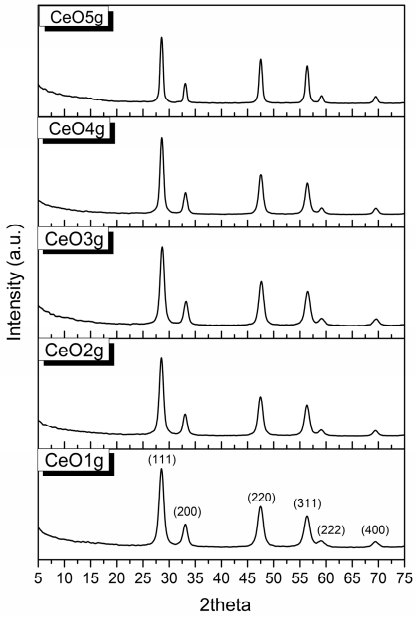


Figure 2. XRD patterns of CeO_2 nanoparticles.

3.3. Scanning Electron Microscopy

The morphology of cerium oxide nanoparticles was evaluated with SEM and the images are presented in Figure 3. Concerning morphology, micrographs exhibit aggregates of spherical particles in the range of 140–300 nm. CeO1g and CeO5g presented a well-defined morphology suggesting better dispersion, compared with the rest of the NPs that showed close contact with the particles within the aggregates. EDS spectrum analysis confirmed that prepared CeO_2 nanoparticles contained elemental cerium and oxygen peaks, without any impurities.

3.4. Transmission Electron Microscopy

The microstructure of the NPs, from the lowest (CeO1g) to the highest (CeO5g) Ce concentration, was investigated using TEM, SAED, and HRTEM imaging modes. Characteristic images recorded from the two samples are illustrated in Figure 4. In particular, the morphology and size of the CeO1g NPs are shown in the TEM image of Figure 4a. The nanoparticles have almost a spherical shape with sizes ranging from 4.5 to 11 nm, with the majority having an average size of 8.5 ± 2.5 nm. The corresponding SAED ring pattern, shown in Figure 4b, depicts the CeO1g crystal structure. The sequence of the diffraction rings, from the inner to the outer, corresponds to the interplanar spacing of {111}, {200}, {220}, {311}, {222}, {400}, and {331} etc. lattice planes of the CeO_2 fluorite structure (cubic F m $\bar{3}$ m). The HRTEM image of an NP, showing its atomic structure projected along the <110> zone axis, is illustrated in Figure 4c. Magnification of the area bounded by the rectangular frame and the corresponding calculated Fast Fourier Transform (FFT) are given as insets. The spacing of the two families of {111} lattice fringes is also indicated. The FFT reveals the special frequencies, decomposed by the HRTEM image, and indicates the characteristic <110> projection of the cubic CeO_2 structure.

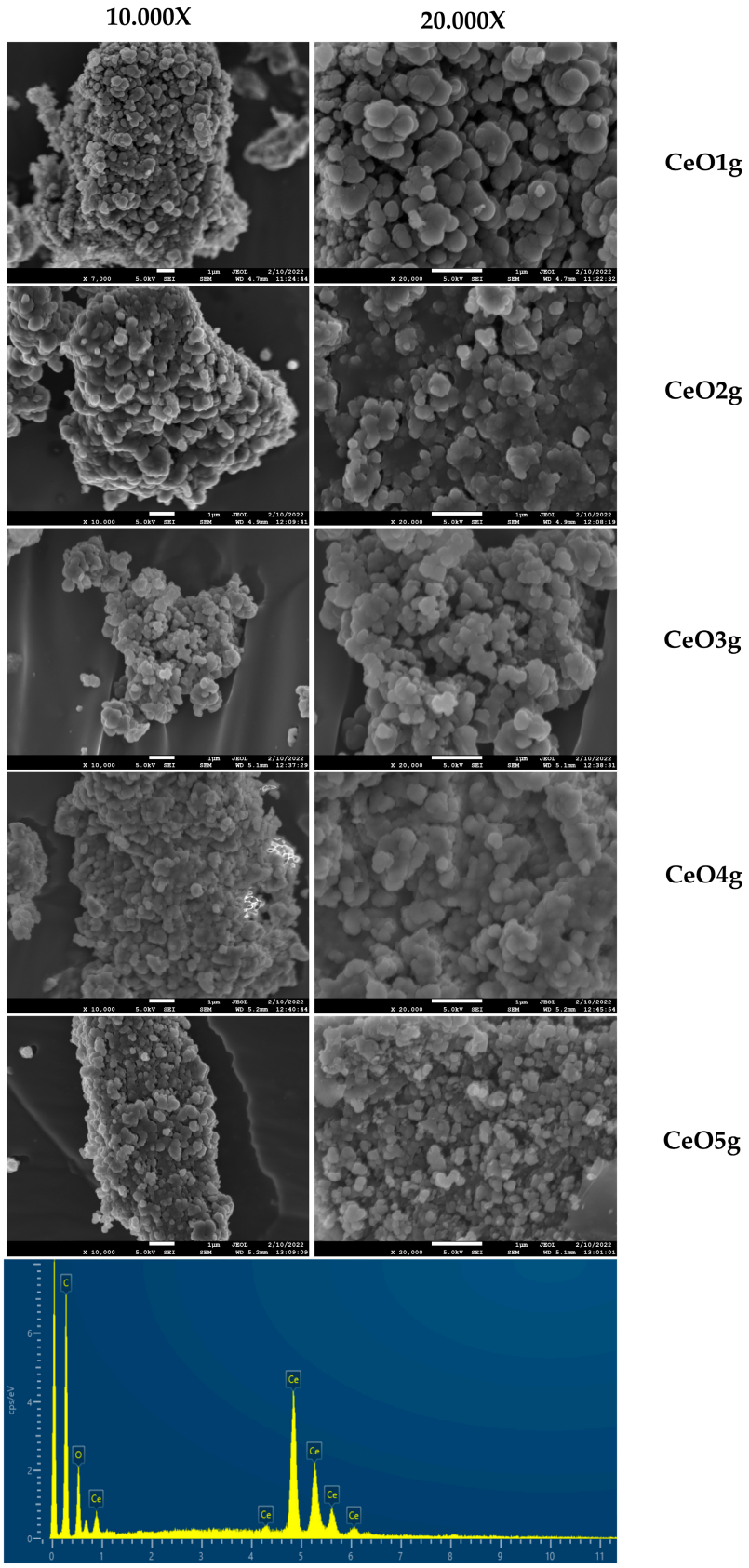


Figure 3. SEM micrographs of synthesized materials and representative EDS spectrum verifying the presence of cerium.

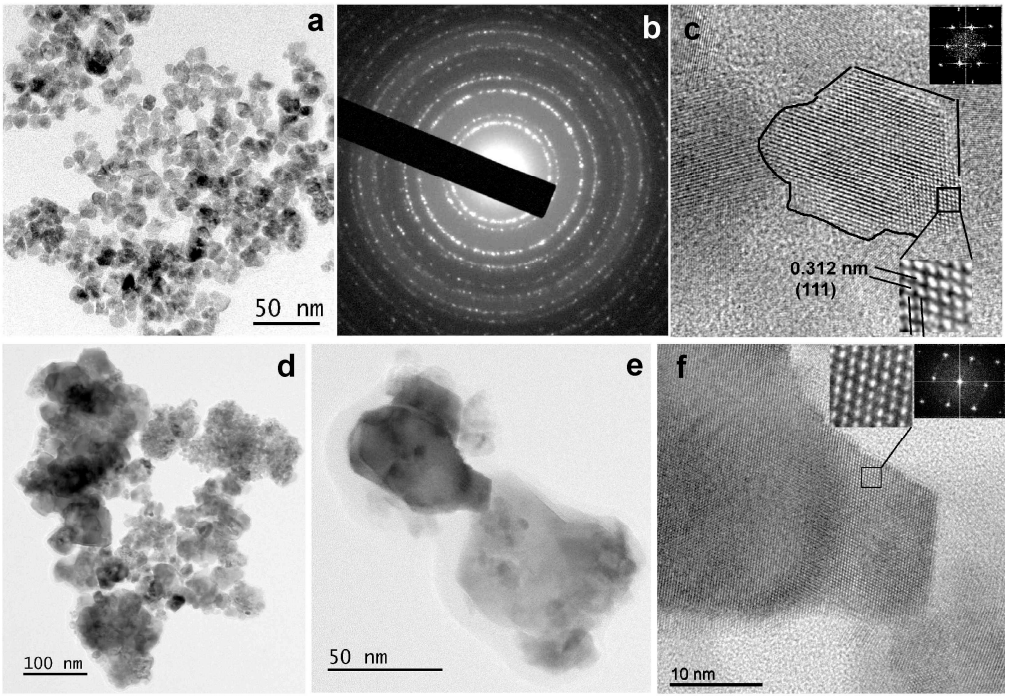


Figure 4. (**a**) TEM image illustrating the NPs recorder from the sample CeO1g. (**b**) the corresponding SAED ring pattern including the sequence of reflections of the cubic CeO_2 fluorite structure. (**c**) HRTEM image of a CeO1g NP with a magnified part, showing the atomic structure viewed along <110> zone axis, and the corresponding FFT as insets. (**d**) TEM image of the NPs consisting of the sample CeO5g. (**e**) TEM image of sample CeO5g illustrating two NPs with an average projected size of about 50 nm. (**f**) HRTEM image obtained from the darker, in contrast, NP of (**e**), viewed along the <110> zone axis. Magnified part of the image showing the two families of {111} lattice fringes and the corresponding FFT are given as insets.

The CeO5g sample comprised two types of crystalline nanoparticles with respect to their size, as displayed in the TEM images of Figure 4d,e. Agglomerations with rather spherical small-size NPs and those with irregular shape and a much larger size compared to the CeO1g sample, being the majority, are observed. The size of the larger NPs is 35 ± 10 nm, although larger than that were also observed as those presented in Figure 4e. Despite the difference in size, all NPs possessed the cubic CeO_2 fluorite structure. The HRTEM image of Figure 4f shows the atomic structure of the darker, in contrast, NP of Figure 4e. The image is viewed along the <110> zone axis and was recorded from the edge area of the NP. The magnified part of the area bounded by the rectangular frame and the corresponding FFT, given as insets, clearly reveals the cubic CeO_2 structure. The lattice fringe spacing, also equal to 0.312 nm, corresponds to the d-spacing of the {111} lattice planes.

3.5. Hemocompatibility Assay

Figure 5 shows the hemocompatibility of CeO_2 NPs after 24 h of incubation at body temperature (37 °C). None of the NPs induce hemolysis at concentrations lower than 500 μg/mL, compared with the positive control ($p < 0.05$). CeO_2 NPs doped with lower gelatin (CeO3g, CeO4g, CeO5g) did not induce lysis in erythrocytes even at the highest tested concentration (1000 μg/mL). In detail, CeO1g appeared to be hemolytic when used at 1000 μg/mL (6% of hemolysis), while the same trend was also observed for CeO2g (8% of hemolysis). When the Ce precursor/gelatin ratio increased, erythrocyte fragility remained low and the NPs presented no hemolytic effect at all in the analyzed concentrations.

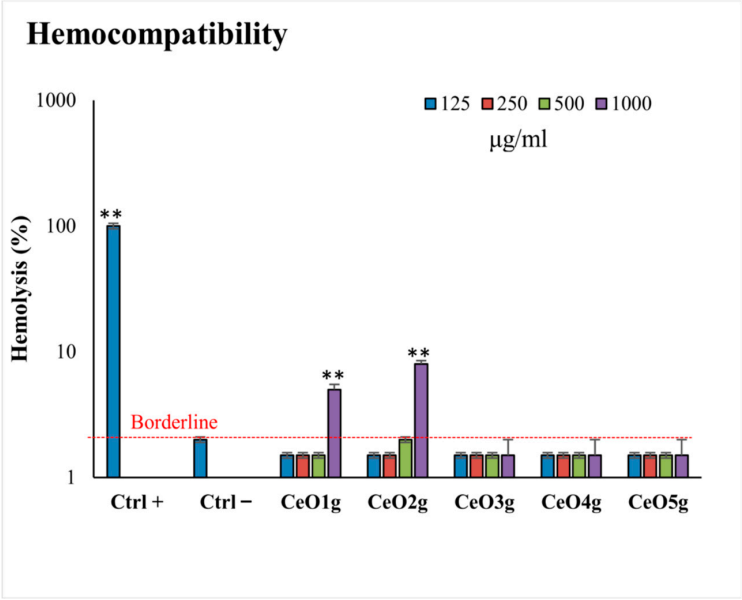


Figure 5. Hemolytic activity (hemocompatibility) of the tested CeO_2 NPs at different concentrations (125–1000 µg/mL). ** indicates a statistically significant difference ($p < 0.001$) between erythrocytes with NPs and negative control of hemolysis (CTRL−).

3.6. Reactive Oxygen Species Assay

Figure 6 presents the ROS levels in erythrocytes after incubation with the different tested concentrations of the CeO_2 NPs (125–1000 µg/mL). CeO2g at all tested concentrations presented the highest amount of ROS levels in comparison to the positive control and the other tested NPs ($p < 0.05$), while CeO4g appeared to promote ROS scavenging. A clear trend was observed towards increased ROS scavenging by increasing the Ce precursor/gelatin ratio, as the CeO_2 NPs with the highest amount of cerium nitrate (CeO4g and CeO5g) presented lower ROS% in erythrocytes compared to the positive control with H_2O_2, indicating a protective role in oxidation conditions ($p < 0.05$).

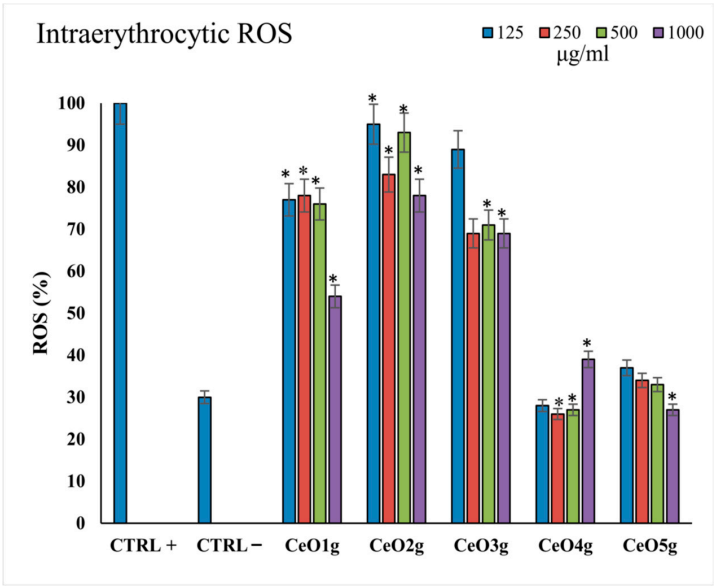


Figure 6. Intracellular ROS (%) levels after 24 h of incubation with the different CeO_2 NPs at all the tested concentrations 125–1000 µg/mL). The lines with * above bars indicate statistically significant differences ($p < 0.05$) of ROS % among the positive controls treated with 10 µM H_2O_2.

4. Discussion

In this study, the synthesis of CeO_2 NPs was successfully performed via the sol-gel method. The interaction between the oxygen atoms in gelatin and the cerium cations allowed the gelatin molecules to first adsorb on the solvated Ce^{3+} ions in water. Due to the oxygen in the air, Ce^{3+} simultaneously switched to Ce^{4+}, changing the original solution's color from colorless to light yellow. Following the sol-gel method with gelatin as a stabilizer and subsequent heat treatment, highly crystallized CeO_2 NPs were developed. The results are encouraging as it was observed that, as the Ce precursor/gelatin ratio increases, the crystallinity raises (Figure 2), as well as the hemocompatibility and the antioxidant activity improve (Figures 5 and 6). According to Darroudi et al., the introduction of gelatin in the sol-gel served as a stabilizing agent for both the initial ions and the final products. In particular, gelatin significantly prevented agglomeration by stabilizing the $Ce(OH)_4$ nuclei and CeO_2 NPs as they were produced by bonding between the carbonyl groups and surface hydroxyls [51]. The use of gelatin has been proposed in many studies for the synthesis of different types of NPs (Table 2). Gao and his team synthesized $LiFePO_4$/C nanocomposites via sol-gel with and without gelatin [64]. Their results showed that, when $LiFePO_4$ was produced using gelatin, the XRD patterns revealed a pure, highly crystalline phase of $LiFePO_4$. However, $LiFePO_4$ produced without gelatin had high levels of impurities (FeP, $LiCO_3$, and Fe_2P), demonstrating that gelatin promotes the production of $LiFePO_4$. In their SEM micrographs, the average particle size of NPs generated with gelatin was around 183 nm. In contrast, the particle size of powders synthesized without gelatin was greater (1–2 μm). This outcome demonstrates that the gelatin-based sol-gel method may successfully adjust particle size as in our study. In another study, Darroudi and his team prepared Ag-NPs in gelatin solutions under UV light irradiation [65]. Gelatin concentrations had a clear impact on the SPR (surface plasmon resonance) bands of silver nanostructures. Also, as the ratio of AgNO/gelatin raised, greater yields of Ag-NPs were produced. Finally, the surface morphology of the finely distributed Ag-NPs was shown by the AFM result to have a dense and evenly packed structure as also revealed in the present study by SEM and TEM. In a previous study, different ratios of gelatin to precursor at different temperatures were examined. It was concluded that the amount of gelatin has an impact on several structural characteristics, such as the uniformity of the size distribution and the size of the particles, including the temperature at which the structures develop. The results showed that with the smallest ratio of gelatin to the precursor (1:1 and 2:1), the formation of a crystalline phase was observed to occur at 550 degrees, while with the largest ratio (3:1), crystallization initiated at 350 degrees. From these data, it can be concluded that gelatin concentration is crucial for the development of crystalline structure as well as for regulating the size of the NPs [66]. These findings agree with our results since with the applied calcination temperature (550 °C), high crystallinity was present in all samples and as the ratio of precursor/gelatin increased, crystallinity slightly increased. This is verified by the presence of more sharp peaks in the XRD diffractogram with the increase of Ce precursor/gelatin ratio (Figure 2). In the XRD pattern of CeO1g, although pure crystalline material was observed, a broadening of the peaks is evidenced. The broadened peaks may be due to the presence of smaller-sized particles [67,68], as was also observed in the present study, where CeO1g samples presented NPs in the range of 4.5–9.5 nm (Figure 4). Similar were the results of Periyat et al. [7], who presented an increase in crystallite size with the calcination temperature and an accompanying broadening of the peaks at low calcination temperatures.

Table 2. Studies investigating the synthesis of CeO_2 NPs and NPs using gelatin.

Studies	Synthesis Method	Nanomaterials	Particle Size	RBCs Compatibility	ROS Scavenging	Calcination Temperature	Greater Precursor/Gelatin Ratio
Synthesis of CeO_2 NPs							
Present study	Sol-gel	CeO_2 NPs	<10 nm	+	+	550 °C	Larger NPs
Periyat 2019 [7]	Sol-gel	CeO_2 NPs	9–13 nm			400 °C 500 °C 600 °C	
Kurian 2014 [69]	Co-precipitation	CeO_2 NPs	4–37 nm			400 °C 700 °C	
	Sol-gel	CeO_2 NPs	27.9–36.9 nm			700 °C	
Gnanam 2011 [70]	Sol-gel	CeO_2 NPs	8 nm			400 °C	
Fudala 2021 [71]	Sol-gel	CeO_2 NPs	10 nm			400 °C	
He 2019 [41]	Sol-gel	CeO_2 NPs	10 nm			500 °C	
Darroudi 2013 [51]	Sol-gel	CeO_2 NPs	<10 nm			120 °C 200 °C 400 °C 600 °C	
Singh 2019 [72]	Co-precipitation	CeO_2 NPs	250–325 nm			350 °C 400 °C 450 °C	
Chen 2010 [73]	Co-precipitation	CeO_2 nanopowders	10 nm 80 nm 100 nm			273 K 473 K 673 K 773 K 873 K 1073 K 1273 K	
Turco 2019 [74]	purchased by Sigma code 544841	CeO_2 NPs	5–40 nm	+	+		

Table 2. *Cont.*

Studies	Synthesis Method	Nanomaterials	Particle Size	RBCs Compatibility	ROS Scavenging	Calcination Temperature	Greater Precursor/Gelatin Ratio
Liu 2009 [75]	thermal decomposition	CeO_2 NPs	~4 nm	+	+	600 °C	
Li 2019 [27]	hydrothermal	CeO_2 nanorods CeO_2 nanocubes CeO_2 nano-octah	9.6 ± 1.2 nm 57.2 ± 17.5 nm 29.1 ± 11.7 nm	+ + +	+ + +		
			Synthesis of NPs using gelatin				
present	Sol-gel	CeO_2 NPs	<10 nm	+	+	550 °C	Larger NPs
Darroudi 2011 [65]	UV irradiation	Ag NPs	18.8 nm			ambient	Larger yields
Azad 2018 [66]	Sol-gel	$LiMn_2O_4$ nanopowders	70 nm			350 °C 550 °C 750 °C 850 °C	Larger NPs
Oliveira 2017 [76]	Sol-gel	Si-Al micro/mesopores				700 °C	
Khorrami 2017 [77]	Sol-gel	KNN-NPs	50 nm 100 nm			500 °C 600 °C 700 °C 800 °C	
Zak 2011 [78]	Sol-gel	ZnO NPs	29 ± 5 nm 40 ± 10 nm 58 ± 15 nm			400 °C 500 °C 600 °C 700 °C	

The sol-gel approach has gained popularity due to its flexibility, its ability to produce high-quality ultrafine nanostructures, its low operating temperature, and its ability to adjust particle size and shape. Many studies utilize the sol-gel method in order to create CeO_2 nanoparticles in a more environmentally friendly manner with similar findings to those found in the current work. In terms of particle size, Manju Kurian compared NPs prepared by the sol-gel method and the coprecipitation method and concluded that with coprecipitation, the average size of CeO_2 nanoparticles was 4–37 nm in contrast to sol-gel using ethylene glycol as a solvent, which was 27.9–36.9 nm [69]. Gnanam et al., synthesized via sol-gel elliptical/spherical CeO_2 nanoparticles with average sizes of ~8 nm [70]. Fudala et al., studied the synthesis of different sizes of CeO_2 nanoparticles by utilizing varying amounts of a precursor using the sol–gel process and concluded that as the concentration of the precursor of cerium increases, the average nanoparticles size decreases, reaching average sizes of less than 100 nm [71]. This finding is in contrast to our study in which the largest Ce precursor amount presented NPs with a larger size (Figure 4). Hong-Wei He et al., synthesized via a sol-gel process a nano CeO_2 hydrosol which consisted of colloids with crystalline face-centered cubic nanostructured cerium dioxide. The particles of CeO_2 were approximately 10 nm in size [79]. Periyat et al. synthesized spherical nanoparticles with an approximate particle size of 9–13 nm [7]. All these studies and many more confirm that sol-gel is a reliable and trustworthy method for particle synthesis in the nanometer scale, as the NPs had a minimum particle size of 4.5 nm, as demonstrated by our TEM study (Figure 4).

According to our results, in relation to the calcination temperature at 550 °C, XRD patterns and SEM/TEM analyses showed that the synthesized nanoparticles had 100% crystallinity (Figure 2) and presented homogeneity as shown in Figures 2–4. Darroudi et al. studied the synthesis of CeO_2 nanoparticles at different heating temperatures (120 °C, 200 °C, 400 °C, and 600 °C) and concluded that with higher calcination temperatures, XRD peaks became sharper, attributing the enhancement of crystallinity to calcination temperature [51]. Periyat et al., ended up with the same results, observing that synthesized CeO_2 nanoparticles at different calcination temperatures (400 °C, 500 °C, and 600 °C) via the sol-gel method showed an increase in crystal size as the temperature increased. With the rising calcination temperature, the surface area of all samples decreased. The greater interparticle pore diameters for larger particles are reflected in the lower values for surface area. Despite differences in size, all samples exhibited a uniform spherical morphology. In the present study, at the highest Ce precursor/gelatin ratio the spherical shape was retained in the smaller particles, however, a more rectangular or irregular morphology was observed in the largest NPs (Figure 4). Singh et al., synthesized ceria by the coprecipitation method at three different temperatures 350 °C, 400 °C, and 450 °C. The results revealed that with the elevation of temperature, the CeO_2 nanoparticles' crystal size increased. Also, the specific surface area seemed to be decreasing as grain size increased, which proves that temperature and crystallinity are proportional, since as one increased, so did the other [72]. Chen et al. studied the crystallite growth in synthesized CeO_2 NPs under various calcinated temperatures. They concluded that as the calcination temperature increased, the smaller particles were progressively integrated into larger ones. Also, the calcination temperature increased the nanoparticles' crystallinity and average crystallite size [73].

Nanotechnology has aided in the prevention, rapid diagnosis, and therapy of many diseases as well as in the development of specific topographical surface formations, such as implant surfaces, with reliable tissue-integrated properties. Blood vessels are damaged during surgery, which causes implant surfaces to come into contact with blood components [28]. Thus, the initiation of potential negative effects on human health is a major worry with regard to the use of NPs in medicinal applications [80]. Designing and creating suitable nanomaterials that do not cause hemolysis and the formation of ROS following administration is an important issue for nanomedicine. The primary purpose of RBCs, which is based on their metabolic nature, is to carry oxygen to all tissues. Red blood cells are continually exposed to ROS under physiological circumstances. It has been noted that

an accumulation of ROS in RBCs might degrade the properties and structure of hemoglobin, reducing its ability to carry oxygen [81]. Numerous investigations revealed that the physicochemical characteristics of NPs can cause erythrocyte damage [82,83]. The erythrocyte membrane's oxidative damage is one process essential to hemolysis. Elevated oxidative stress results in cell damage since erythrocytes do not produce SOD and catalase, which are two essential enzymes for ROS scavenging. Various substances, including magnesium hydroxide, carbon-based nanoparticles [84], silver [85], and gold [86], have been examined for their hemolytic potential. Each of these compounds has a unique hemolytic property, highlighting the necessity of determining the vital hemocompatibility factors before applying these nanomaterials to medicinal applications. Particularly, the hemocompatibility of implants coated with NPs is a subject of considerable research. Titanium implants were coated with TiO_2 nanotubes, calcium phosphate coating, and a phospholipid (POPC) film by Mehdi Kazemzadeh-Narbat et al. According to hemocompatibility results, there were relatively low hemolysis levels on various implant surfaces. Since it did not statistically differ from the PBS control, the coating did not trigger RBC lysis [87]. As coatings for titanium implants, Mariana Prodana et al. employed carbon nanotubes, hydroxyapatite, and TiO_2 nanotubes. None of the materials induced hemolytic reactions, according to the results of hemolysis. When compared to the material covered in HA, the addition of carbon nanotubes raised the hemolysis percentage, though not to a point that is harmful to the human body [88]. Hendrik Vögeling et al. claim that poly(lactic-co-glycolic acid) PLGA nanoparticles loaded with norfloxacin (NFX) were utilized to figure out the effectiveness of these NPs as antibacterial agents. The hemolytic results showed a slight increase in haemolysis rates when PLGA/NFX nanoparticles were compared to controls [89]. Li et al. synthesized and studied the impact of different shaped CeO NPs (nanorod, nanocube, and nano-octahedron CeO_2) on Ti surfaces in relation to their anti-inflammatory and antibacterial response. Comparing the results concerning their antioxidant capacity, octahedron CeO_2 had the greatest results leading to successful scavenging of ROS in contrast to nanorods which showed noneffective anti-inflammatory activity. All samples exhibited excellent hemocompatibility, biocompatibility, and biosafety. Finally, regarding antibacterial efficacy, cube-CeO_2, and octa-CeO_2 showed inhibition of bacterial adhesion (*P. gingivalis*, *F. nucleatum*, *S. sanguinis*) [27]. Our findings demonstrated that CeO_2 nanoparticles with a higher amount of cerium precursor (CeO3g, CeO4g, and CeO5g) did not cause hemolysis or alter the morphology of erythrocytes at all tested concentrations (Figure 5). Also, CeO4g and CeO5g presented ROS scavenging capacity at all tested concentrations (Figure 6). This finding might be attributed to the mixed NPs population observed at least for CeO5g, which included NPs with higher diameters. It has been reported that ROS is highly associated with the diameter of NPs, and this is observed in different types of NPs [90]. The mechanism behind this phenomenon was the cellular uptake which increased as the size decreased. Nano CeO_2 antioxidant activity may help to maintain the membrane's integrity after coming in contact with erythrocytes since it imitates the actions of SOD and catalase by acting as an ROS scavenger. The reported scavenging activity of synthesized CeO_2 nanoparticles in the present research work was consistent with prior research findings [53]. A recent study that assessed CeO_2 nanoparticles on hemostasis, showed that CeO_2 did not induce hemolysis on red blood cells (RBC) at all tested concentrations. Also, under oxidative stress, CeO_2 reduced ROS formation induced by H_2O_2 [74]. Liu et al. studied the influence of CNPs on RBCs at hyperthermic conditions. The results showed that CeO_2-treated cells had a much lower rate of apoptosis than the control cells. They also examined how CeO_2 nanoparticles affected the generation of ROS, leading to the conclusion that red blood cells subjected to hyperthermia decreased ROS generation and improved apoptosis even at extremely low concentrations of CNPs [29].

In the present study, modulation of only one parameter (precursor amount) was employed to clarify the role of gelatin in the shape and crystallinity of the synthesized NPs. However, other parameters such as pH, synthesis, and calcination temperature may further affect the final structural, physicochemical, and biological properties of NPs. The authors

are currently evaluating NPs' antibacterial activity against *P. intermedia* and *P.gingivalis*, two bacteria species related to periimplantitis, and, although preliminary results show promising antibacterial action, further in vitro studies are needed to clearly demonstrate their capability of inhibiting bacteria growth, either as planktonic bacteria or in biofilms. Careful monitoring of these parameters may result in optimum NPs, based on the desired biomedical applications.

5. Conclusions

The current study discusses the synthesis and characterization of CeO_2 nanoparticles based on the ratio between cerium precursor and gelatin used as stabilizing agents. TEM analysis showed NPs to have a size below 10 nm. However, with the increase of cerium precursor and decrease of gelatin, particles became larger, reaching 25–50 nm, revealing the important aspect of having the proper quantity of stabilizer during sol-gel synthesis of CeO_2 NPs. XRD analysis and HRTEM determined the high crystallinity of the nanoparticles and confirmed the dependence of crystallinity on the gelatin amount. Hemocompatibility and ROS assay performed using erythrocytes showed that the NPs with the highest ratio of Ce precursor/gelatin are hemocompatible and there was no cell death even at higher concentrations (1000 μg/mL). Also, they presented ROS scavenging properties indicating a protective role for CeO_2 NPs in oxidation conditions. The amount of gelatin affected the morphology of particles and specifically as the ratio of Ce precursor/gelatin decreased, particle size also decreased and better homogeneity was achieved. However, at the same time erythrocyte toxicity occurred, while ROS scavenging was reduced, which was suggested as more appropriate in biomedical applications for the NPs with the highest amount of Ce precursor. Future studies should focus on other synthesis parameters to optimize the properties of CeO_2 NPs for different biomedical applications.

Author Contributions: Conceptualization, M.E.I., G.K.P. and E.K.; methodology, M.E.I., G.K.P., I.T. (Ioannis Tsamesidis), I.C., N.F., I.T. (Ioannis Tsiaoussis), P.K. and E.L; formal analysis, M.E.I., G.K.P., I.T. (Ioannis Tsamesidis), I.C., N.F., I.T. (Ioannis Tsiaoussis), P.K. and E.L.; investigation, M.E.I., G.K.P., I.T. (Ioannis Tsamesidis), I.C., N.F., I.T. (Ioannis Tsiaoussis), P.K. and E.L.; resources, E.K.; data curation, M.E.I., G.K.P., I.T. (Ioannis Tsamesidis), N.F., I.T. (Ioannis Tsiaoussis) and P.K.; writing—original draft preparation, M.E.I., I.T. (Ioannis Tsamesidis) and I.T. (Ioannis Tsamesidis); writing—review and editing, M.E.I., G.K.P., I.T. (Ioannis Tsamesidis), P.K. and E.K.; supervision, E.K. All authors have read and agreed to the published version of the manuscript.

Funding: This research received no external funding.

Institutional Review Board Statement: The study was conducted according to the guidelines of the Declaration of Helsinki and approved by the Ethics Committee of the School of Dentistry, Aristotle University of Thessaloniki (#110/10-2-2021).

Informed Consent Statement: Informed consent was obtained from blood donors.

Data Availability Statement: All data are presented in the article.

Acknowledgments: The authors would like to acknowledge Chrysanthi Papoulia for carrying out the SEM measurements and the Advanced Materials and Devices Laboratory, School of Physics, Faculty of Sciences, Aristotle University of Thessaloniki for providing access to perform the FTIR, SEM, and XRD measurements. All TEM characterization was performed at the Electron Microscopy and Structural Characterization of Materials, School of Physics, Faculty of Sciences, Aristotle University of Thessaloniki.

Conflicts of Interest: The authors declare no conflict of interest.

References

1. Science, N.; Council, T. National Nanotechnology Initiative—Leading To the Next Industrial Revolution. *Microscale Thermophys. Eng.* **2000**, *4*, 205–212.
2. Thakur, S.; Patil, P. Rapid synthesis of cerium oxide nanoparticles with superior humidity-sensing performance. *Sens. Actuators B Chem.* **2014**, *194*, 260–268. [CrossRef]

3. Pal, S.L.; Jana, U.; Manna, P.K.; Mohanta, G.P.; Manavalan, R. Nanoparticle: An overview of preparation and characterization. *J. Appl. Pharm. Sci.* **2011**, *1*, 228–234.
4. Singh, K.R.B.; Nayak, V.; Sarkar, T.; Singh, R.P. Cerium oxide nanoparticles: Properties, biosynthesis and biomedical application. *RSC Adv.* **2020**, *10*, 27194–27214. [CrossRef]
5. Thakur, N.; Manna, P.; Das, J. Synthesis and biomedical applications of nanoceria, a redox active nanoparticle. *J. Nanobiotech.* **2019**, *17*, 1–27. [CrossRef]
6. Ramasamy, V.; Mohana, V.; Suresh, G. The synthesis and characterization of undoped and Ni doped CeO_2 nanoparticles using sol-gel method. *Int. J. Mater. Sci.* **2017**, *12*, 2.
7. Periyat, P.; Laffir, F.; Tofail, S.A.M.; Magner, E. A facile aqueous sol-gel method for high surface area nanocrystalline CeO_2. *RSC Adv.* **2011**, *1*, 1794–1798. [CrossRef]
8. Stoianov, O.O.; Ivanov, V.K.; Shcherbakov, A.B.; Stoyanova, I.V.; Chivireva, N.A.; Antonovich, V.P. Determination of cerium(III) and cerium(IV) in nanodisperse ceria by chemical methods. *Russ. J. Inorg. Chem.* **2014**, *59*, 15–23. [CrossRef]
9. Keren Jiang, K.J. Fabrication and Catalytic Property of Cerium Oxide Nanomaterials. Master Thesis, University of Nebraska, Lincoln, NE, USA, 2011. Available online: https://digitalcommons.unl.edu/chemistrydiss/22.
10. Cam, T.S.; Omarov, S.O.; Chebanenko, M.I.; Izotova, S.G.; Popkov, V.I. Recent progress in the synthesis of CeO_2-based nanocatalysts towards efficient oxidation of CO. *J. Sci. Adv. Mater. Devices* **2022**, *7*, 100399. [CrossRef]
11. Murali, A.; Lan, Y.P.; Sohn, H.Y. Effect of oxygen vacancies in non-stoichiometric ceria on its photocatalytic properties. *Nano-Structures and Nano-Objects* **2019**, *18*, 100257. [CrossRef]
12. Younis, A.; Chu, D.; Li, S. Cerium Oxide Nanostructures and their Applications. In *Functionalized Nanomaterials*; IntechOpen: Rijeka, Croatia, 2016.
13. Sun, C.; Li, H.; Chen, L. Nanostructured ceria-based materials: Synthesis, properties, and applications. *Energy Environ. Sci.* **2012**, *5*, 8475–8505. [CrossRef]
14. Ma, Y.; Gao, W.; Zhang, Z.; Zhang, S.; Tian, Z.; Liu, Y.; Ho, J.C.; Qu, Y. Regulating the surface of nanoceria and its applications in heterogeneous catalysis. *Surf. Sci. Rep.* **2018**, *73*, 1–36. [CrossRef]
15. Korsvik, C.; Patil, S.; Seal, S.; Self, W.T. Superoxide dismutase mimetic properties exhibited by vacancy engineered ceria nanoparticles. *Chem. Commun.* **2007**, 1056–1058. [CrossRef]
16. Saifi, M.A.; Seal, S.; Godugu, C. Nanoceria, the versatile nanoparticles: Promising biomedical applications. *J. Control. Release* **2021**, *338*, 164–189. [CrossRef]
17. Celardo, I.; Pedersen, J.Z.; Traversa, E.; Ghibelli, L. Pharmacological potential of cerium oxide nanoparticles. *Nanoscale* **2011**, *3*, 1411–1420. [CrossRef]
18. Melo, M.A.S.; Weir, M.D.; Li, F.; Cheng, L.; Zhang, K.; Xu, H.H.K. Control of biofilm at the tooth-restoration bonding interface: A question for antibacterial monomers? A critical review. *Rev. Adhes. Adhes.* **2017**, *5*, 303–323. [CrossRef]
19. Nedeljkovic, I.; Teughels, W.; De Munck, J.; Van Meerbeek, B.; Van Landuyt, K.L. Is secondary caries with composites a material-based problem? *Dent. Mater.* **2015**, *31*, e247–e277. [CrossRef]
20. Varghese, E.J.; Sihivahanan, D.; Venkatesh, K.V. Development of Novel Antimicrobial Dental Composite Resin with Nano Cerium Oxide Fillers. *Int. J. Biomater.* **2022**, *2022*, 3912290. [CrossRef]
21. Balhaddad, A.A.; Kansara, A.A.; Hidan, D.; Weir, M.D.; Xu, H.H.K.; Melo, M.A.S. Toward dental caries: Exploring nanoparticle-based platforms and calcium phosphate compounds for dental restorative materials. *Bioact. Mater.* **2019**, *4*, 43–55. [CrossRef]
22. Van Nieuwenhuysen, J.P.; D'Hoore, W.; Carvalho, J.; Qvist, V. Long-term evaluation of extensive restorations in permanent teeth. *J. Dent.* **2003**, *31*, 395–405. [CrossRef]
23. Talreja, P.S.; Gayathri, G.V.; Mehta, D.S. Treatment of an early failing implant by guided bone regeneration using resorbable collagen membrane and bioactive glass. *J. Indian Soc. Periodontol.* **2013**, *17*, 131–136. [CrossRef]
24. Yazdani, J.; Hajizadeh, S.; Kananizadeh, Y.; Pourghasem-Gargari, B.; Ghojazadeh, M. Evaluation of changes in paraclinical indexes due to intermaxillary fixation. *J. Anal. Res. Clin. Med.* **2015**, *3*, 138–142. [CrossRef]
25. Oshida, Y.; Tuna, E.B.; Aktören, O.; Gençay, K. Dental implant systems. *Int. J. Mol. Sci.* **2010**, *11*, 1580–1678. [CrossRef]
26. Parnia, F.; Yazdani, J.; Javaherzadeh, V.; Dizaj, S.M. Overview of Nanoparticle Coating of Dental Implants for Enhanced Osseointegration and Antimicrobial Purposes. *J. Pharm. Pharm. Sci.* **2017**, *20*, 148–160. [CrossRef]
27. Li, X.; Qi, M.; Sun, X.; Weir, M.D.; Tay, F.R.; Oates, T.W.; Dong, B.; Zhou, Y.; Wang, L.; Xu, H.H.K. Surface treatments on titanium implants via nanostructured ceria for antibacterial and anti-inflammatory capabilities. *Acta Biomater.* **2019**, *94*, 627–643. [CrossRef]
28. Lavenus, S.; Louarn, G.; Layrolle, P. Nanotechnology and Dental Implants. *Int. J. Biomater.* **2010**, *2010*, 915327. [CrossRef]
29. Liu, T.; Han, S.; Pang, M.; Li, J.; Wang, J.; Luo, X.; Wang, Y.; Liu, Z.; Yang, X.; Ye, Z. Cerium oxide nanoparticles protect red blood cells from hyperthermia-induced damages. *J. Biomater. Appl.* **2021**, *36*, 36–44. [CrossRef]
30. Abbas, F.; Iqbal, J.; Jan, T.; Badshah, N.; Mansoor, Q.; Ismail, M. Structural, morphological, Raman, optical, magnetic, and antibacterial characteristics of CeO_2 nanostructures. *Int. J. Miner. Metall. Mater.* **2016**, *23*, 102–108. [CrossRef]
31. Rosenbloom, R.G.; Tinanoff, N. Salivary *Streptococcus mutans* levels in patients before, during, and after orthodontic treatment. *Am. J. Orthod. Dentofac. Orthop.* **1991**, *100*, 35–37. [CrossRef]
32. Gorelick, L.; Geiger, A.M.; John, A. Incidence of white spot Jbmxation after bonding and banding. *Am. J. Orthod.* **1982**, *81*, 93–98. [CrossRef]
33. Bishara, S.E.; Ostby, A.W. White Spot Lesions: Formation, Prevention, and Treatment. *Semin. Orthod.* **2008**, *14*, 174–182. [CrossRef]

34. O'Reilly, M.M.; Featherstone, J.D.B. Demineralization and remineralization around orthodontic appliances: An in vivo study. *Am. J. Orthod. Dentofac. Orthop.* **1987**, *92*, 33–40. [CrossRef]
35. Zholobak, N.M.; Ivanov, V.K.; Shcherbakov, A.B. Interaction of nanoceria with microorganisms. Elsevier: Amsterdam, The Netherlands, 2016; ISBN 9780323428873.
36. Arumugam, A.; Karthikeyan, C.; Haja Hameed, A.S.; Gopinath, K.; Gowri, S.; Karthika, V. Synthesis of cerium oxide nanoparticles using Gloriosa superba L. leaf extract and their structural, optical and antibacterial properties. *Mater. Sci. Eng. C* **2015**, *49*, 408–415. [CrossRef]
37. Zeyons, O.; Thill, A.; Chauvat, F.; Menguy, N.; Cassier-Chauvat, C.; ORéAR, C.; Daraspe, J.; Auffan, M.; Rose, J.; Spalla, O. Direct and indirect CeO_2 nanoparticles toxicity for Escherichia coli and Synechocystis. *Nanotoxicology* **2009**, *3*, 284–295. [CrossRef]
38. Pelletier, D.A.; Suresh, A.K.; Holton, G.A.; McKeown, C.K.; Wang, W.; Gu, B.; Mortensen, N.P.; Allison, D.P.; Joy, D.C.; Allison, M.R.; et al. Effects of engineered cerium oxide nanoparticles on bacterial growth and viability. *Appl. Environ. Microbiol.* **2010**, *76*, 7981–7989. [CrossRef]
39. Qamar, M.A.; Shahid, S.; Javed, M. Synthesis of dynamic g-C3N4/Fe@ZnO nanocomposites for environmental remediation applications. *Ceram. Int.* **2020**, *46*, 22171–22180. [CrossRef]
40. Paiva, C.N.; Bozza, M.T. Are reactive oxygen species always detrimental to pathogens? *Antioxid. Redox Signal.* **2014**, *20*, 1000–1037. [CrossRef]
41. Kang, H.; Buchman, J.T.; Rodriguez, R.S.; Ring, H.L.; He, J.; Bantz, K.C.; Haynes, C.L. Stabilization of Silver and Gold Nanoparticles: Preservation and Improvement of Plasmonic Functionalities. *Chem. Rev.* **2019**, *119*, 664–699. [CrossRef]
42. El-Nahhal, I.M.; Elmanama, A.A.; Amara, N.; Qodih, F.S.; Selmane, M.; Chehimi, M.M. The efficacy of surfactants in stabilizing coating of nano-structured CuO particles onto the surface of cotton fibers and their antimicrobial activity. *Mater. Chem. Phys.* **2018**, *215*, 221–228. [CrossRef]
43. Cai, Z.; Fu, J.; Du, P.; Zhao, X.; Hao, X.; Liu, W.; Zhao, D. Reduction of nitrobenzene in aqueous and soil phases using carboxymethyl cellulose stabilized zero-valent iron nanoparticles. *Chem. Eng. J.* **2018**, *332*, 227–236. [CrossRef]
44. Blinov, A.V.; Gvozdenko, A.A.; Yasnaya, M.A.; Blinova, A.A.; Kravtsov, A.A.; Krandievsky, S.O.; Kramarenko, V.N. Synthesing and studying the structure of nanoscale copper (II) oxide stabilized by polyethylene glycol. *Her. Bauman Moscow State Tech. Univ. Ser. Nat. Sci.* **2020**, 56–70.
45. Dippon, U.; Pabst, S.; Klitzke, S. Colloidal stabilization of CeO_2 nanomaterials with polyacrylic acid, polyvinyl alcohol or natural organic matter. *Sci. Total Environ.* **2018**, *645*, 1153–1158. [CrossRef]
46. Ivanov, V.K.; Polezhaeva, O.S.; Shaporev, A.S.; Baranchikov, A.E.; Shcherbakov, A.B.; Usatenko, A.V. Synthesis and thermal stability of nanocrystalline ceria sols stabilized by citric and polyacrylic acids. *Russ. J. Inorg. Chem.* **2010**, *55*, 328–332. [CrossRef]
47. Gvozdenko, A.A.; Siddiqui, S.A.; Blinov, A.V.; Golik, A.B.; Nagdalian, A.A.; Maglakelidze, D.G.; Statsenko, E.N.; Pirogov, M.A.; Blinova, A.A.; Sizonenko, M.N.; et al. Synthesis of CuO nanoparticles stabilized with gelatin for potential use in food packaging applications. *Sci. Rep.* **2022**, *12*, 12843. [CrossRef]
48. Likos, C.N.; Vaynberg, K.A.; Löwen, H.; Wagner, N.J. Colloidal stabilization by adsorbed gelatin. *Langmuir* **2000**, *16*, 4100–4108. [CrossRef]
49. Darroudi, M.; Ahmad, M.B.; Abdullah, A.H.; Ibrahim, N.A. Green synthesis and characterization of gelatin-based and sugar-reduced silver nanoparticles. *Int. J. Nanomedicine* **2011**, *6*, 569–574. [CrossRef]
50. Wang, Y.C.; Gunasekaran, S. Spectroscopic and microscopic investigation of gold nanoparticle nucleation and growth mechanisms using gelatin as a stabilizer. *J. Nanoparticle Res.* **2012**, *14*, 1200. [CrossRef]
51. Darroudi, M.; Hakimi, M.; Sarani, M.; Kazemi Oskuee, R.; Khorsand Zak, A.; Gholami, L. Facile synthesis, characterization, and evaluation of neurotoxicity effect of cerium oxide nanoparticles. *Ceram. Int.* **2013**, *39*, 6917–6921. [CrossRef]
52. Wierzbinski, K.R.; Szymanski, T.; Rozwadowska, N.; Rybka, J.D.; Zimna, A.; Zalewski, T.; Nowicka-Bauer, K.; Malcher, A.; Nowaczyk, M.; Krupinski, M.; et al. Potential use of superparamagnetic iron oxide nanoparticles for in vitro and in vivo bioimaging of human myoblasts. *Sci. Rep.* **2018**, *8*, 1–17. [CrossRef]
53. Tsamesidis, I.; Gkiliopoulos, D.; Pouroutzidou, G.K.; Lymperaki, E.; Papoulia, C.; Reybier, K.; Perio, P.; Paraskevopoulos, K.M.; Kontonasaki, E.; Theocharidou, A. Effect of artemisinin-loaded mesoporous cerium-doped calcium silicate nanopowder on cell proliferation of human periodontal ligament fibroblasts. *Nanomaterials* **2021**, *11*, 2189. [CrossRef]
54. Tsamesidis, I.; Pouroutzidou, G.K.; Lymperaki, E.; Kazeli, K.; Lioutas, C.B.; Christodoulou, E.; Perio, P.; Reybier, K.; Pantaleo, A.; Kontonasaki, E. Effect of ion doping in silica-based nanoparticles on the hemolytic and oxidative activity in contact with human erythrocytes. *Chem. Biol. Interact.* **2020**, *318*, 108974. [CrossRef]
55. Tumkur, P.P.; Gunasekaran, N.K.; Lamani, B.R.; Nazario Bayon, N.; Prabhakaran, K.; Hall, J.C.; Ramesh, G.T. Cerium Oxide Nanoparticles: Synthesis and Characterization for Biosafe Applications. *Nanomanufacturing* **2021**, *1*, 176–189. [CrossRef]
56. Wu, N.-C.; Shi, E.-W.; Zheng, Y.-Q.; Li, W.-J. Effect of pH of Medium on Hydrothermal Synthesis of Nanocrystalline Cerium(IV) Oxide Powders. *J. Am. Ceram. Soc.* **2002**, *85*, 2462–2468. [CrossRef]
57. Farahmandjou, M.; Farahmandjou, M.; Zarinkamar, M.; Firoozabadi, T.P. Synthesis of Cerium Oxide (CeO_2) nanoparticles using simple CO-precipitation method Article in Revista Mexicana de Fisica · Synthesis of Cerium Oxide (CeO_2) nanoparticles using simple CO-precipitation method. *Rev. Mex. Física* **2016**, *62*, 496–499.

58. Akbari, A.; Khammar, M.; Taherzadeh, D.; Rajabian, A.; Khorsand Zak, A.; Darroudi, M. Zinc-doped cerium oxide nanoparticles: Sol-gel synthesis, characterization, and investigation of their in vitro cytotoxicity effects. *J. Mol. Struct.* **2017**, *1149*, 771–776. [CrossRef]
59. Sifontes, A.B.; Gonzalez, G.; Ochoa, J.L.; Tovar, L.M.; Zoltan, T.; Cañizales, E. Chitosan as template for the synthesis of ceria nanoparticles. *Mater. Res. Bull.* **2011**, *46*, 1794–1799. [CrossRef]
60. Yue, L.; Zhang, X.M. Structural characterization and photocatalytic behaviors of doped CeO_2 nanoparticles. *J. Alloys Compd.* **2009**, *475*, 702–705. [CrossRef]
61. Balamurugan, A.; Sudha, M.; Surendhiran, S.; Anandarasu, R.; Ravikumar, S.; Syed Khadar, Y.A. Hydrothermal synthesis of samarium (Sm) doped cerium oxide (CeO_2) nanoparticles: Characterization and antibacterial activity. *Mater. Today Proc.* **2019**, *26*, 3588–3594. [CrossRef]
62. An, X.; Shi, X.; Zhang, H.; Yao, Y.; Wang, G.; Yang, Q.; Xia, L.; Sun, X. An electrochemical immunosensor based on a combined amplification strategy with the GO-CS/CeO_2-CS nanocomposite for the detection of aflatoxin M1. *New J. Chem.* **2020**, *44*, 1362–1370. [CrossRef]
63. Fan, C.; Pan, W.; Wang, W.; Rao, Q.; Yan, A.; Chen, S.; Zheng, A.; Li, Y.; Huang, B.; Sun, Y. Sol-gel synthesis of cerium dioxide nanoparticles coated with stimuli-responsive components and the application for conversion of d-(−)-fructose into platform molecules. *J. Sol-Gel Sci. Technol.* **2018**, *88*, 141–162. [CrossRef]
64. Gao, M.; Liu, N.; Li, Z.; Wang, W.; Li, C.; Zhang, H.; Chen, Y.; Yu, Z.; Huang, Y. A gelatin-based sol-gel procedure to synthesize the LiFePO4/C nanocomposite for lithium ion batteries. *Solid State Ionics* **2014**, *258*, 8–12. [CrossRef]
65. Darroudi, M.; Ahmad, M.B.; Zak, A.K.; Zamiri, R.; Hakimi, M. Fabrication and characterization of gelatin stabilized silver nanoparticles under UV-Light. *Int. J. Mol. Sci.* **2011**, *12*, 6346–6356. [CrossRef]
66. Azad, N.; Arabi, H.; Ghorbani, S.R.; Davodi, A. The effect of gelatin as a chelating agent on the synthesis and characterization of LiMn2O4 nanopowders prepared via sol–gel method. *J. Sol-Gel Sci. Technol.* **2018**, *88*, 465–473. [CrossRef]
67. Nanosains, J. Derivation of Scherrer Relation Using an Approach in Basic Physics Course. *Nano* **2008**, *1*, 28–32.
68. Ungár, T. Microstructural parameters from X-ray diffraction peak broadening. *Scr. Mater.* **2004**, *51*, 777–781. [CrossRef]
69. Kurian, M.; Kunjachan, C. Investigation of size dependency on lattice strain of nanoceria particles synthesised by wet chemical methods. *Int. Nano Lett.* **2014**, *4*, 73–80. [CrossRef]
70. Gnanam, S.; Rajendran, V. Synthesis of CeO_2 or α-Mn_2O_3 nanoparticles via sol-gel process and their optical properties. *J. Sol-Gel Sci. Technol.* **2011**, *58*, 62–69. [CrossRef]
71. Fudala, A.S.; Salih, W.M.; Alkazaz, F.F. Synthesis different sizes of cerium oxide CeO_2 nanoparticles by using different concentrations of precursor via sol–gel method. *Mater. Today Proc.* **2021**, *49*, 2786–2792. [CrossRef]
72. Singh, R.D.; Koli, P.B.; Jagdale, B.S.; Patil, A.V. Effect of firing temperature on structural and electrical parameters of synthesized CeO_2 thick films. *SN Appl. Sci.* **2019**, *1*, 1–9. [CrossRef]
73. Chen, J.C.; Chen, W.C.; Tien, Y.C.; Shih, C.J. Effect of calcination temperature on the crystallite growth of cerium oxide nanopowders prepared by the co-precipitation process. *J. Alloys Compd.* **2010**, *496*, 364–369. [CrossRef]
74. Del Turco, S.; Ciofani, G.; Cappello, V.; Parlanti, P.; Gemmi, M.; Caselli, C.; Ragusa, R.; Papa, A.; Battaglia, D.; Sabatino, L.; et al. Effects of cerium oxide nanoparticles on hemostasis: Coagulation, platelets, and vascular endothelial cells. *J. Biomed. Mater. Res.—Part A* **2019**, *107*, 1551–1562. [CrossRef]
75. Liu, J.; Wang, F.; Dewil, R. CeO_2 nanocrystalline-supported palladium chloride: An effective catalyst for selective oxidation of alcohols by Oxygen. *Catal. Letters* **2009**, *130*, 448–454. [CrossRef]
76. De Oliveira, A.S.K.; Paulista, A.P.F.; De Alencar, A.E.V.; Braga, T.P. Gelatin Template Synthesis of Aluminum Oxide and/or Silicon Oxide Containing Micro/Mesopores Using the Proteic Sol-Gel Method. *J. Nanomater.* **2017**, *2017*, 2504796. [CrossRef]
77. Khorrami, G.H.; Kompany, A.; Khorsand Zak, A. A facile sol-gel approach to synthesize KNN nanoparticles at low temperature. *Mater. Lett.* **2013**, *110*, 172–175. [CrossRef]
78. Zak, A.K.; Majid, W.H.A.; Darroudi, M.; Yousefi, R. Synthesis and characterization of ZnO nanoparticles prepared in gelatin media. *Mater. Lett.* **2011**, *65*, 70–73. [CrossRef]
79. He, H.W.; Wu, X.Q.; Ren, W.; Shi, P.; Yao, X.; Song, Z.T. Synthesis of crystalline cerium dioxide hydrosol by a sol-gel method. *Ceram. Int.* **2012**, *38*, S501–S504. [CrossRef]
80. Jong, W.H.D.; Paul, J.B. Drug delivery and nanoparticles: Applications and hazards. *Int. J. Nanomedicine* **2008**, *3*, 133–149. [CrossRef]
81. Ellsworth, M.L. The red blood cell as an oxygen sensor: What is the evidence? *Acta Physiol. Scand.* **2000**, *168*, 551–559. [CrossRef]
82. Chen, L.Q.; Fang, L.; Ling, J.; Ding, C.Z.; Kang, B.; Huang, C.Z. Nanotoxicity of silver nanoparticles to red blood cells: Size dependent adsorption, uptake, and hemolytic activity. *Chem. Res. Toxicol.* **2015**, *28*, 501–509. [CrossRef]
83. de Luna, L.A.V.; Martinez, D.S.T.; Alves, O.L. Assessing the Erythrocyte Toxicity of Nanomaterials: From Current Methods to Biomolecular Surface Chemistry Interactions. *Nanotoxicol. Mater. Methodol. Assess.* **2014**, 347–361.
84. Fedel, M. Hemocompatibility of Carbon Nanostructures. *C — J. Carbon Res.* **2020**, *6*, 12. [CrossRef]
85. Avitabile, E.; Senes, N.; D'Avino, C.; Tsamesidis, I.; Pinna, A.; Medici, S.; Pantaleo, A. The potential antimalarial efficacy of hemocompatible silver nanoparticles from Artemisia species against *P. falciparum* parasite. *PLoS ONE* **2020**, *15*, 1–17. [CrossRef]
86. Khan, I.; Vishwakarma, S.K.; Khan, A.A.; Ramakrishnan, G.; Dutta, J.R. In vitro hemocompatability evaluation of gold nanoparticles capped with *Lactobacillus plantarum* derived lipase. *Clin. Hemorheol. Microcirc.* **2018**, *69*, 197–205. [CrossRef]

87. Kazemzadeh-Narbat, M.; Lai, B.F.L.; Ding, C.; Kizhakkedathu, J.N.; Hancock, R.E.W.; Wang, R. Multilayered coating on titanium for controlled release of antimicrobial peptides for the prevention of implant-associated infections. *Biomaterials* **2013**, *34*, 5969–5977. [CrossRef]
88. Prodana, M.; Duta, M.; Ionita, D.; Bojin, D.; Stan, M.S.; Dinischiotu, A.; Demetrescu, I. A new complex ceramic coating with carbon nanotubes, hydroxyapatite and TiO2 nanotubes on Ti surface for biomedical applications. *Ceram. Int.* **2015**, *41*, 6318–6325. [CrossRef]
89. Vögeling, H.; Duse, L.; Seitz, B.S.; Plenagl, N.; Wojcik, M.; Pinnapireddy, S.R.; Bakowsky, U. Multilayer Bacteriostatic Coating for Surface Modified Titanium Implants. *Phys. Status Solidi Appl. Mater. Sci.* **2018**, *215*, 1700844. [CrossRef]
90. Yu, Z.; Li, Q.; Wang, J.; Yu, Y.; Wang, Y.; Zhou, Q.; Li, P. Reactive Oxygen Species-Related Nanoparticle Toxicity in the Biomedical Field. *Nanoscale Res. Lett.* **2020**, *15*, 1–14. [CrossRef]

Disclaimer/Publisher's Note: The statements, opinions and data contained in all publications are solely those of the individual author(s) and contributor(s) and not of MDPI and/or the editor(s). MDPI and/or the editor(s) disclaim responsibility for any injury to people or property resulting from any ideas, methods, instructions or products referred to in the content.